Ultrasound Probe and Needle-Guide Calibration for Robotic Ultrasound Scanning and Needle Targeting

Chunwoo Kim, Doyoung Chang, Doru Petrisor, Gregory Chirikjian, Misop Han, and Dan Stoianovici

Abstract— **Image-to-robot registration is a typical step for robotic image-guided interventions. If the imaging device uses a portable imaging probe that is held by a robot, this registration is constant and has been commonly named probe calibration. The same applies to probes tracked by a position measurement device.**

We report a calibration method for two dimensional (2D) ultrasound probes using robotic manipulation and a planar calibration rig. Moreover, a needle-guide that is attached to the probe is also calibrated for ultrasound-guided needle targeting.

The method is applied to a transrectal ultrasound (TRUS) probe for robot-assisted prostate biopsy. Validation experiments include TRUS-guided needle targeting accuracy tests. The paper outlines the entire process from the calibration to image-guided targeting.

Freehand TRUS-guided prostate biopsy is the primary method of diagnosing prostate cancer, with over 1.2 million procedures performed annually in the US alone. However, freehand biopsy is a highly challenging procedure with subjective quality control. As such, biopsy devices are emerging to assist the physician. Here, we present a method that uses robotic TRUS manipulation.

A 2D TRUS probe is supported by a 4 degree of freedom (DoF) robot. The robot performs ultrasound scanning, enabling 3D reconstructions. Based on the images the robot orients a needle-guide on target for biopsy. The biopsy is acquired manually through the guide.

In-vitro tests showed that the 3D images were geometrically accurate, and image-based needle targeting accuracy was 1.55mm. These validate the probe calibration presented and the overall robotic system for needle targeting. Targeting accuracy is sufficient for targeting small, clinically significant prostatic cancer lesions, but actual in-vivo targeting will include additional error components that will have to be determined.

Index Terms — **ultrasound calibration, registration, needle-guide calibration, image-guided robot, prostate biopsy**

I. INTRODUCTION

PROSTATE cancer (PCa) is the second most common cause of cancer deaths among American men. In 2012 alone, 241,740 newly diagnosed PCa cases and 28,170 PCa deaths are estimated [1]. The primary method for diagnosing PCa is transrectal ultrasound (TRUS) guided prostate biopsy. However, standard gray-scale ultrasound imaging provides minimal PCa specific information, being unreliable in differentiating normal prostate gland from cancerous tissue. Accordingly, TRUS-guided biopsies are not specifically targeting cancer suspicious regions, relying instead on non-targeted, systematic schemata for cancer detection and characterization. The TRUS probe is typically moved freehand by a physician who attempts to place the needle so that the biopsy cores are uniformly distributed throughout the prostate according to a systematic, sextant biopsy schema (typically 12 cores, Left/Right x Medial/Lateral x Apex/Mid/Base). However, this is a challenging procedure because it is beyond regular hand-eye coordination tasks. The motion is inverted, ultrasound images are typically 2D and may be difficult to interpret, and one hand has to handle the TRUS probe while the other is engaged with the biopsy needle. Studies have shown that biopsy samples are often clustered, miss regions, and do not follow the uniform schema [2-4]. Accordingly, with freehand TRUS-guided biopsy both overdiagnosis of clinically insignificant cancer and underdiagnosis of potentially lethal cancer exist in the population at risk of PCa [5, 6].

One of the proposed technologies to improve prostate biopsy is TRUS probe position tracking. Tracking allows ultrasound scanning to generate 3D images from a set of 2D slices [7, 8]. These include electromagnetic trackers [9, 10], and encoded arms [11, 12]. A robotic device also gives automated motion for scanning and subsequent image-guided targeting.

Yet trackers and robots require registration to the images, which is the identification of the constant transformation between the 2D image slice and the probe body coordinate systems. This mandatory procedure is called probe calibration [13]. The way in which the calibrations have been performed for devices is often presented briefly in the literature.

Several publications have focused on ultrasound calibration [14-18]. Commonly, these methods use calibration rigs and tracked probes, and several require rig tracking [14, 16]. The rigs are typically constructed of strings [14-16] or planes [17,
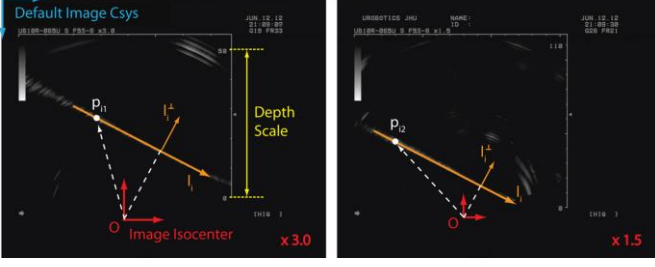
Figure 1: 4-DoF TRUS Robot: Image, probe, and robot coordinate systems (CSys)

18] submersed in a water basin. In ultrasound, strings generate points and planes generate lines that may be easier to detect by automated means [13]. Imaged features of the rigs and calibration parameters must satisfy a set of constraint equations. Typically, these are optimized for the parameters based on experimental images.

Previous ultrasound calibration methods could be applied to calibrate a robot manipulated probe. However, in applying these methods with the robot we observed that the methods could be improved. We used a similar planar surface mockup submersed in a water tank. But we observed that the calibration problem may be simplified by a sequential approach that separates the scale, isocenter, orientation, and offset parameter identifications. Typically, all parameters have been identified globally and employed non-linear optimization methods. In our case, we further simplified the identification by using a linearization of the constraint equations.

To target a needle based on the ultrasound, a needle-guide is commonly attached to the probe. Often, the location and direction of the needle-guide with respect to the probe is assumed to correspond to the CAD (Computer Aided Design), descriptions being typically omitted in other papers. Here, we also present an image-to-model calibration of the needle-guide based on the calibrated 3D ultrasound. The accuracies of the image and needle-guide calibrations are validated by in-vitro imaging and targeting tests.

II. Calibration Method

A. TRUS Robot

We have developed two similar endocavity probe manipulators (TRUS robots) with 3 and 4-DoF [7]. The calibration methods described can be used with either version. The experiments presented in this paper were performed with the 4-DoF robot, shown in Figure 1. These 4-DoF are kinematically equivalent to human manipulation of a TRUS probe. The robot consists of a Remote Center of Motion (RCM) mechanism to pivot the probe and an additional translation for probe insertion [19]. Details about the construction of the robot and kinematics are described in a prior publication [7].

Custom software integrated with the visualization software Amira (Visage Imaging, San Diego CA.) was developed for

image guidance. The robot control runs on a separate computer, communicating with the image-guidance software over a TCP/IP connection. This modular design reduces computational load and separates controller components that implement robotic safety features [7].

The robot control and image-guidance software allows scanning with 2D image slices through robotic motion for 3D reconstruction and subsequent image-guidance. A required component, however, is the probe calibration that is to be determined.

B. Ultrasound Probe Calibration Problem

As shown in Figure 1, the configuration of the coordinate frames of the images acquired by the TRUS probe manipulated by the TRUS Robot is given by $F(\theta_i)\,{}^P_I G$, where:

$$F(\theta_i) = \begin{bmatrix} R_i & \vec{t}_i \\ \vec{0}^T & 1 \end{bmatrix} \qquad \text{(Eq. 1)}$$

is the forward kinematics of the robot describing the configuration of the probe coordinate system P with respect to the robot base coordinate system at joint angle θ_i, and ${}^P_I G$ is a probe calibration constant matrix describing the configuration of the image coordinate system I with respect to the probe coordinate system P.

The probe calibration matrix may be expressed as:

$$ {}^P_I G = \begin{bmatrix} X & \vec{x} \\ \vec{0}^T & 1 \end{bmatrix} \begin{bmatrix} s_x & 0 & 0 & 0 \\ 0 & s_y & 0 & 0 \\ 0 & 0 & 0 & 0 \\ 0 & 0 & 0 & 1 \end{bmatrix} = \begin{bmatrix} X & \vec{x} \\ \vec{0}^T & 1 \end{bmatrix} S \quad \text{(Eq. 2)} $$

where, s_x and s_y are the scale factors (mm/pixel) in x and y directions of the image and S is the scaling matrix, X is a rotation matrix and $\vec{x}$ is an offset between the two systems. The calibration maps any point ${}^I\vec{p} = [u, v, 0]^T$ in the ultrasound image measured in pixels to a point ${}^P\vec{p} = {}^P_I G\,{}^I\vec{p} = [x, y, z]^T$ in the probe coordinate system measured in mm.

The scope of the calibration is to identify the calibration parameters $(X, \vec{x}, s_x, s_y)$ from the combined robot-probe system based on imaging experiments that image a calibration rig from multiple robot positions $(F(\theta_i))$. Our calibration rig is a plane submersed in a water tank. Scale, orientation and offset parameters are sequentially identified as follows:

C. Calibration of Scale and Image Isocenter

Ultrasound images are commonly captured by digitizing the output video signal from the ultrasound machine using a frame grabber. The resulting pixels may not be square, and the scale factors should be identified in both directions.

Each s_x and s_y can be determined from the mm/pixel ratio of the scale bars available in the image (Figure 2). Precision is highest if the longest feature of the scale bar is used. If the scale-bars provided by the ultrasound manufacturer may not be reliable, a calibration rig with known physical dimensions should be imaged instead.

Ultrasound machines present several depth settings that

Figure 2: Image scale and scale invariant point O defining the origin of the image coordinate frame.

result in different scale factors. Therefore the scale factors must be identified for all depth settings used. The depth setting also changes the offset $\vec{x}$, unless the origin of image coordinate system is conveniently set at the image isocenter ($\vec{O}$ in Figure 2). Physically this corresponds to the center of the transducer array.

To identify the isocenter, images of the planar calibration rig (lines) are obtained at two depth settings (S_1 and S_2) from several dissimilar (imaged lines not parallel) robot orientations. For each orientation i, the imaged lines at the two scales are parallel ($\vec{l}_i$). As such, the pixel distance from the isocenter $\vec{O}$ to line 1 is $(\vec{p}_{i1} - \vec{O})^T \vec{l}_i^\perp$, where $\vec{p}_{i1}$ is a point on line 1, and $\vec{l}_i^\perp$ is the direction normal to $\vec{l}_i$, and similarly for line 2. These distances are proportional to the depth settings, therefore:

$$(\vec{p}_{i1} - \vec{O})^T S_1 \vec{l}_i^\perp = (\vec{p}_{i2} - \vec{O})^T S_2 \vec{l}_i^\perp \qquad \text{(Eq. 3)}$$

In this scalar equation the two unknowns are the pixel coordinates of the isocenter, $\vec{O} = [u_o, v_o, 0]^T$. The measurements of more than two orientations, lead to an over determined system:

$$\begin{bmatrix} (S_1 - S_2)\vec{l}_i^\perp \\ \vdots \end{bmatrix} \vec{O} = \begin{bmatrix} (S_1\vec{p}_{i1} - S_2\vec{p}_{i2})^T\vec{l}_i^\perp \\ \vdots \end{bmatrix} \qquad \text{(Eq. 4)}$$

which can be solved for $\vec{O}$. Alternatively, $\vec{O}$ can be determined from two robot positions that lead to nearly orthogonal imaged lines, by intersecting the corresponding parallel lines that pass through $\vec{O}$. The calibrated scales S are applied to all subsequent calibrations, so that the units of the points and lines selected in the image are directly expressed in mm.

D. Calibration of Image Orientation

When the plane of the calibration rig is imaged from a joint angle θ_i, the imaged line $\vec{l}_i$ can be expressed in the robot base coordinate as:

$$\vec{L}_i = F(\theta_i)_I^P G \vec{l}_i = R_i X \vec{l}_i \qquad \text{(Eq. 5)}$$

For three robot orientations, the corresponding lines $\vec{L}_i, \vec{L}_j, \vec{L}_k$ are constrained to the same plane, therefore:

$$\vec{L}_i^T (\vec{L}_j \times \vec{L}_k) = \vec{l}_i^T X^T R_i^T (R_j X \hat{l}_j X^T R_j^T R_k X \vec{l}_k) = 0 \qquad \text{(Eq. 6)}$$

where, the operator $\wedge$ converts a vector into the corresponding skew-symmetric matrix such that $\hat{a}\vec{x} = \vec{a} \times \vec{x}$. This constraint equation is non-linear. Instead of using a non-linear optimization method as commonly done by others [14, 16-18], we use a simpler method based on linearization. An initial estimate of the image orientation X_0 may be calculated from the CAD model of the ultrasound probe. The actual X will be slightly rotated by a vector $\vec{\delta}$. For a small rotations $|\delta|$, the image orientation can be approximated as:

$$X = X_0 e^{\hat{\delta}} \approx X_0(I + \hat{\delta}) \qquad \text{(Eq. 7)}$$

This approximation linearizes the constrain equations:

$$\vec{l}_i^T(I + \delta)^T Q_{ji}^T(I + \delta)\hat{l}_j(I + \delta)^T Q_{jk}(I + \delta)\vec{l}_k \qquad \text{(Eq. 8)}$$

where $Q_{ji} = X_0^T R_j^T R_i X_0$ and $Q_{jk} = X_0^T R_j^T R_k X_0$. Expanding and neglecting higher order terms in $\hat{\delta}$ leads to the following linear system:

$$\begin{bmatrix} \vec{a}_{ji}^T\widehat{b_{jk}}(I - Q_{ji}) + \vec{b}_{ji}^T\widehat{a_{jk}}(I - Q_{jk}) \\ \vdots \end{bmatrix} \delta = \begin{bmatrix} \alpha_{ijk} \\ \vdots \end{bmatrix} \text{ (Eq. 9)}$$

where: $a_{ji} = Q_{ji}\vec{l}_i$, $b_{ji} = \hat{l}_j Q_{ji}\vec{l}_i$, $\alpha_{ijk} = \vec{l}_i^T Q_{ij}\hat{l}_j Q_{jk}\vec{l}_k$

For n robot orientations the number of combinations of 3 imaged lines is C_3^n. These can be used to formulate an over determined linear system, that can be solved for δ, determining the image orientation X. This procedure is iterated by updating the initial estimate to $X_0 = X$ until the convergence is reached ($|\delta|$ becomes very small).

E. Calibration of Image Offset

This calibration uses the same set of n images used for the calibration of image orientation. With the orientation X , calibrated, the set of lines on the calibration rig plane, $\vec{L}_i$, are now known. The normal of the plane $\vec{n}$ can be determined as a null space of set of $\vec{L}_i$, by the singular value decomposition of the stacked $\vec{L}_i$ matrix.

The robot space position of any point ${}^I\vec{p}_i$ selected on a line in the image is:

$${}^R\vec{p}_i = R_i X {}^I\vec{p}_i + R_i\vec{x} + \vec{t}_i \qquad \text{(Eq. 10)}$$

Taking two such points for different joint angles (i and j)

$$\vec{n}^T({}^B\vec{p}_i - {}^B\vec{p}_j) = 0 \qquad \text{(Eq. 11)}$$

since both points belong to the rig plane. For n robot orientations the number of combinations of 2 points is C_2^n. These can be used to formulate an over determined linear system:

$$\begin{bmatrix} \vec{n}^T(R_i - R_j) \\ \vdots \end{bmatrix}\vec{x} = \begin{bmatrix} \vec{n}^T(R_i X {}^I\vec{p}_j - R_j X {}^I\vec{p}_i + \vec{t}_j - \vec{t}_i) \\ \vdots \end{bmatrix} \text{ (12)}$$

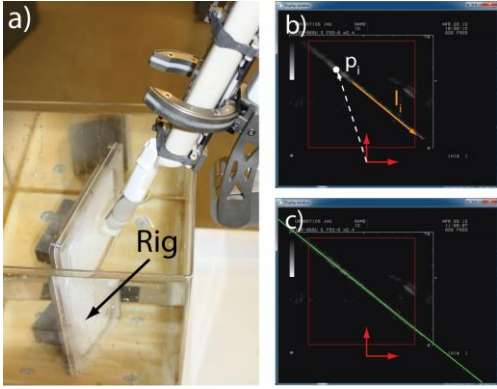which can be solved for $\vec{x}$ by least squares.

Figure 3: a) Probe calibration a) Setup
b) Image of the rig and c) Detected line

III. CALIBRATION EXPERIMENTS

A. Calibration of the TRUS Probe

Figure 3a shows the probe calibration experimental setup with a UB10R-065U (Shimadzu Precision Instruments, Torrance, CA) TRUS probe supported by the 4-DoF TRUS Robot and the plane rig submersed in the water tank. The plane rig is made of thin (0.53mm) plastic sheet. The sheet was roughened with sand paper to increase the reflection of the ultrasound to the transceiver. Experimentally, this showed a clearer image of the plane (line, Figure 3b). The ultrasound video signal was captured in a 720x576 resolution with 59/54 pixel aspect ratio.

To detect the line in the image, this is first eroded to sharpen the line, and pixels belonging to the line were detected by edge detection. A line was then fitted to the detected pixels (Figure 3c) using the RANSAC method.

First the scales in both directions were calibrated as shown in Section II.C using two different depth settings and the image isocenter was determined from 3 robot orientations.

The thickness of the imaged line is related to the beam thickness of the TRUS probe and its incidence angle to the rig plane and corresponding decrease in reflection. As the incidence angle increases (beam more parallel to the plane), the imaged line becomes wider and dimmer. In our case, the range of orientation was limited by a 20° incidence angle. For the rotation and offset calibrations, we have used a total of $n = 24$ robot orientations.

B. Calibration of the Needle-Guide

Once the probe is calibrated the TRUS images are localized in the robot space. The robot may then scan a region of interest to collect image slice-position pairs. These may be used for 3-D image reconstruction. Accordingly, the resulting 3-D images are referenced relative to the robot coordinate space. To implement TRUS-guided needle targeting, an additional calibration of the needle-guide attached to the TRUS probe is needed, as described below.

The calibration consists of identifying the direction of the needle-guide ($^P\vec{g}$) and a position of its reference point ($^P\vec{q}$) (Figure 1).

To calibrate the needle-guide the location of the inserted
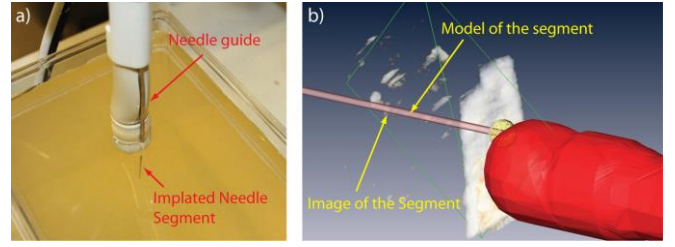
Figure 4: Needle-guide calibration showing
a) the needle segment implanted in the gelatin
b) superimposed needle segment image and model
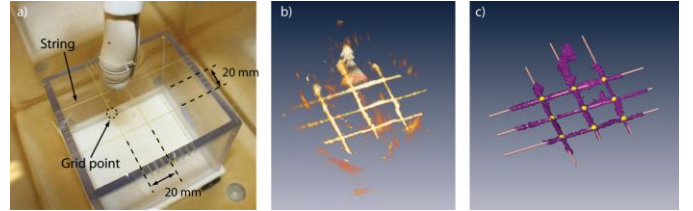
Figure 5: Probe Calibration Accuracy Measurement.
a) Experiment setup b) 3D ultrasound image of
the test mockup and c) Fitted string and intersection

needle should be imaged. But when the needle is inserted the probe may not be moved to acquire its image, because this would also move the needle. As such, rather than imaging the needle itself, we implanted a marker segment through the needle and left it in place so that it can be imaged, as follows.

For this, the probe was instrumented with an 18Ga needle-guide and a calibration needle (18Ga x 200mm trocar needle with symmetric, diamond point) was fully inserted into the gelatin through the guide. Then, a 25 mm long segment of an 18Ga stylet was implanted inside the gelatin through the trocar, in a similar way as it is done for brachytherapy seeds, by backing up the trocar while holding the stylet. Doing so leaves the implanted marker aligned along the direction $^P\vec{g}$ of the needle guide and the distal end at the location of the needle point $^P\vec{q}$.

Scanning the implanted marker shows its 3-D ultrasound image (Figure 4a). Image-to-model registration between the image of the marker and the model of the needle gives the $^R\vec{g}$ and $^R\vec{q}$ needle calibration parameters. The location of the needle model may be calculated based on the position of the robot, as $^P\vec{g} = F(\theta_i)^{-1}\,{}^R\vec{g}$ and $^P\vec{q} = F(\theta_i)^{-1}\,{}^R\vec{q}$. The result show the needle model and marker image superimposed, as shown in Figure 4b.

For other needle lengths, the point of the needle $\vec{q}'$ can be calculated by an offset λ in the $^R\vec{g}$ direction as $\vec{q}' = \vec{q} + \lambda\vec{g}$, where λ is the length difference relative to the calibration needle.

IV. VALIDATION EXPERIMENTS

A. Probe Calibration Accuracy

The accuracy of the probe calibration was verified by imaging a string mockup of known geometry and comparing the acquired image with its CAD model. The mockup consists of 6
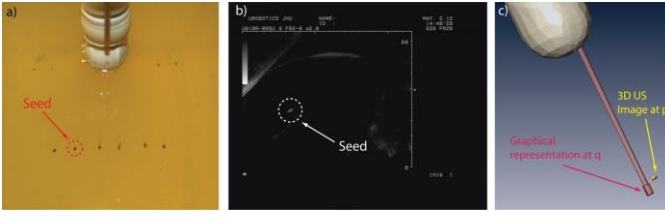
Figure 6: Reversed Targeting Accuracy Measurement.
a) Experiment setup after implanting seeds
b) Ultrasound image showing the implanted seed.
c) Location of $^{R}\vec{p}$ and $^{R}\vec{q}$

strings (made of Φ0.36mm fishing line) forming a 3 by 3 orthogonal grid with 20mm x 20mm spacing (Figure 5a). The mockup was submersed in a water basin and the robot scanned the strings for 3D imaging (Figure 5b). The image was then segmented by thresholding and the strings were reconstructed into a surface (Figure 5c). The six strings defining the grid were fitted to the reconstructed surface and the locations of their nine intersection points were calculated. Then, the angle between all pairs of strings from the image and the CAD model (0°or 90°) were compared. Similarly, the distance between all pairs of intersection points were also compared. For both the angular and linear measures, accuracy was defined as the average of the differences, and precision as the corresponding standard deviations, as usual.

B. Reversed Targeting Accuracy

Validation of the image guided targeting accuracy was performed in two experiments which we termed Direct and Reversed Targeting. Direct Targeting is an image-guided targeting accuracy experiment approach, where physical, visible targets are identified from the image and targeted.

On the other hand, in Reversed Targeting the physical targets are not existent prior to targeting. Instead, these are digitally defined and marked by implanted markers. Their planned vs. actual locations are then compared by imaging.

For the reversed targeting experiment, the robot implanted 12 markers in a gelatin base (Figure 6a) at the target defined by different robot orientation (Table 1). The markers were implanted as described in the section III.B. The markers were made of angel hair spaghetti noodle (Φ0.83mm) cut in 3mm segments. The noodles were found to show lesser artifacts than metals in ultrasound (Figure 6b). The space of the implanted markers was then scanned in ultrasound. The location of the markers calculated from the forward kinematics ($^{R}\vec{q} = F(\theta)\,^{P}\vec{q}$) and their imaged locations ($^{R}\vec{p} = F(\theta)\,^{P}_{I}G\,^{I}\vec{p}_{i}$) were compared. Accuracy was calculated as the average of the magnitude of differences between $\vec{p}$ and $\vec{q}$ ($|^{R}\vec{p} - {}^{R}\vec{q}|$) over all 12 markers, and precision was the corresponding standard deviation.

C. Direct Targeting Accuracy

A gelatin mockup with 6 hyperechoic inclusions (Figure 7a) was made and the center of the inclusions were targeted with the robot under ultrasound-guidance. Gelatin was used for the base material of the mockup. Cylindrical (Φ4.8 x 8.3mm, volume 1.5mL, with rounded tip) inclusions were made of agar

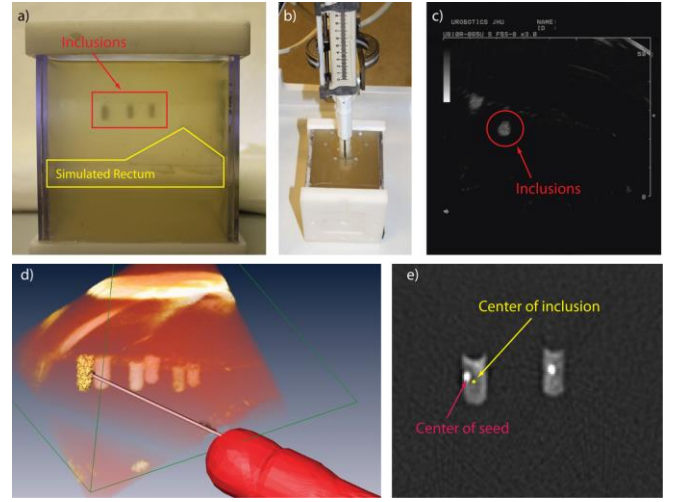Figure 7: Direct Targeting Accuracy Measurement.
a) Mockup b) Targeting setup c) 2D ultrasound image slice
d) 3D ultrasound images and e) CT image slice

(Sigma-Aldrich St. Louis MO.), condensed milk, and glass microspheres (P2043SL, Cospheric LLC, Santa Barbara CA.) for higher echogenicity. Indeed, these inclusions are highly visible in ultrasound (Figure 7c), as described in [20].

The cavity of the mockup was filled with water to provide acoustic coupling (Figure 7b). A rotary scan (about the probe axis) was performed to acquire the 3D ultrasound image. Each inclusion was segmented by thresholding and reconstructed into a surface. The centroid of each inclusion was targeted with the needle point (Figure 7d). Since the 3D image is in robot coordinates, the joint angles were simply generated by inverse kinematics. To mark the location of the targeted needle, markers were implanted as described in the section III.B. These markers were Φ 0.72 x 5mm cylinders made of ceramic material. The ceramic was chosen for further imaging with Computed Tomography (CT), due to its high density relative to the surrounding gelatin.

The mockup was then scanned in CT. The accuracy of needle placement was defined as the average distance (norm of the error vector) between the implanted marker and the targeted point of the inclusion, measured in CT.

V. RESULTS

A. Probe Calibration Accuracy

The angles between the $C_2^6 = 15$ pairs of string measured from their images agreed with their true value within 0.08° with a precision of 0.46°. The distance between the $C_2^9 = 36$ pairs of intersection points measured from their images agreed with their true value within 0.06 mm with a precision of 0.40 mm. These show that the ultrasound scan follows closely the imaged environment, as shown in Figure 5c.

B. Reversed Targeting Accuracy

A graphic representation of the marker positions calculated from the forward kinematics ($\vec{q}$) and its image ($\vec{p}$) is shown in Figure 6c. The reversed targeting accuracy, average magnitude of distance between p and q, was 2.36mm with a precision of

0.937mm. The X, Y, and Z error components in the robot coordinate system are included in Table 1.

Table 1: Reverse targeting accuracy results

Robot Orientation [°]			$^{R}\vec{p} - {}^{R}\vec{q}$ [mm]			
Ry	Rx	Rz	X	Y	Z	Norm
-20	-15	-30	0.690	-0.296	-1.328	1.525
-20	-15	30	0.374	-0.463	0.866	1.051
0	-15	-30	0.045	-1.170	-1.457	1.869
0	-15	30	-0.906	-2.182	-1.711	2.917
20	-15	-30	-0.886	-0.021	-1.409	1.664
20	-15	30	-1.863	-1.756	-2.041	3.274
-20	15	-30	3.944	1.404	-1.355	4.400
-20	15	30	1.112	0.498	-1.895	2.253
0	15	-30	1.019	1.641	-1.889	2.702
0	15	30	-1.427	0.3585	-1.922	2.421
20	15	-30	0.260	1.848	-2.064	2.783
20	15	30	-0.572	0.372	-1.235	1.411
Accuracy			0.149	0.019	-1.453	2.356
Precision			1.528	1.283	0.789	0.937

C. Direct Targeting Accuracy

Figure 7e shows a CT image slice through one of the inclusions and its implanted marker. The direct targeting accuracy, indicating the overall robot-assisted ultrasound guided needle targeting accuracy, was 1.55mm with a precision of 0.55mm.

VI. DISCUSSION AND CONCLUSIONS

While ultrasound has been commonly used freehand, an important recent trend has been to instrument the ultrasound probe with position tracking devices for ultrasound scanning and subsequent ultrasound-guided interventions. Robotic probe manipulation adds controlled motion for scanning and steady positioning for targeting that could impact accuracy. To take advantage of these new methods, however, the localization of images and needle-guide relative to probe must be known.

Our ultrasound calibration uses a simple planar calibration rig and robotic motion. The calibration is performed sequentially for its scale, orientation, and offset components, simplifying the identification by reducing the number of parameter per step. The orientation calibration is further simplified by using a new mathematical formulation of the constraint equation which is solved by linearization instead of the conventional non-linear optimization. Our validation experiments show that 3D scanned images are reconstructed accurately.

While the methods have been derived for robot manipulated probes, these are directly applicable to position tracked probes, such as magnetic trackers. Yet, the calibration results are to be used with the same device. Specifically, the calibration derived with a robot could not directly be used with a tracker, or vice-versa. The resulting calibration mapping is relative to the robot frame, or the tracker. The robot is not a calibration instrument, but is part of the system.

We also present a calibration method for a needle-guide that is typically attached to the probe using an image-to-model method. Overall, this paper outlines the entire formulation and experimental procedure from calibration to image-guided targeting.

The validation experiments have been structured in what we term as Direct and Reversed targeting. Direct targeting is the common image-guided targeting approach that follows the natural workflow of image-guided interventions. A target visible in the image is aimed ("see then target").

The Reversed, on the other hand, is not a factual targeting, but rather a correlation of the digitally defined target and its actual image. In this approach markers are implanted at known locations and imaged thereafter ("target then see").

Both targeting experiments methods give equivalent validation measures, but the Reversed may help in the development stages because the image-to-robot registration is not required prior to targeting. This enables image-based processing such as the calibration to be performed offline, after the images. These may be essential advantages when using CT or MRI (magnetic resonance imaging) guidance, which are less accessible. Moreover, the Reversed Targeting can also be done without a special mockup.

We have tested our system using both targeting experiments under ultrasound guidance, and in addition used CT to validate the direct targeting. Reversed and direct targeting results show 2.36mm and 1.55mm accuracy, respectively. The better result under CT was expected because of its superior measurement resolution and image quality. Since the experiments are equivalent, the 1.55mm accuracy reflects a closer estimate of the targeting performance.

Table 1 shows that the largest reversed targeting error component was in the Z direction. This was expected because the Z direction was close to the marker implant direction and markers are known to shift when placed through the trocar, as seen in "seed migration" in brachytherapy. Therefore, the needle point targeting accuracy, before implanting the markers was likely <1.55mm.

Overall, these validation experiments demonstrate that the calibration methods were accurate. For the prostate biopsy application, these results suggest that the overall TRUS Robot system may be sufficiently accurate to target clinically significant (0.5mL sphere, 5mm radius) PCa tumors. However, this study was performed in-vitro and under idealized conditions. Most importantly, the probe was carefully kept out of contact with the imaged objects by using water for acoustic coupling. While this was appropriate to validate the works, in a typical clinical setting coupling is achieved with ultrasound gel and the probe is pressed to maintain the contact, which can displace and deform the prostate. As such, the actual targeting will include additional error components that will have to be determined.

REFERENCES

[1] R. Siegel, D. Naishadham, and A. Jemal, "Cancer statistics, 2012," *CA Cancer J Clin*, vol. 62, pp. 10-29, 2012.
[2] P. Mozer, M. Baumann, G. Chevreau, A. Moreau-Gaudry, S. Bart, R. Renard-Penna, E. Comperat, P. Conort, M. O. Bitker, E. Chartier-Kastler, F. Richard, and J. Troccaz, "Mapping of transrectal ultrasonographic

prostate biopsies: quality control and learning curve assessment by image processing," *J Ultrasound Med*, vol. 28, pp. 455-60, 2009.

[3] B. Turkbey, S. Xu, J. Kruecker, J. Locklin, Y. Pang, M. Bernardo, M. J. Merino, B. J. Wood, P. L. Choyke, and P. A. Pinto, "Documenting the location of prostate biopsies with image fusion," *BJU Int*, vol. 107, pp. 53-7, 2011.

[4] M. Han, D. Chang, C. Kim, B. J. Lee, Y. Zuo, H. J. Kim, D. Petrisor, B. Trock, A. W. Partin, R. Rodriguez, H. B. Carter, M. Allaf, J. Kim, and D. Stoianovici, "Geometric Evaluation of Systematic Transrectal Ultrasound Guided Prostate Biopsy," *Journal of Urology*, vol. 188, pp. 2404-9, 2012. http://urobotics.urology.jhu.edu/pub/2012-han-jurol.pdf

[5] G. J. Kelloff, P. Choyke, and D. S. Coffey, "Challenges in clinical prostate cancer: role of imaging," *AJR Am J Roentgenol*, vol. 192, pp. 1455-70, 2009.

[6] D. Stoianovici, "Technology Advances for Prostate Biopsy and Needle Therapies. Editorial.," *Journal of Urology*, vol. 188, pp. 1074-5, 2012. http://urobotics.urology.jhu.edu/pub/2012-stoianovici-jurol.pdf

[7] D. Stoianovici, C. Kim, F. Schäfer, C.-M. Huang, Y. Zuo, D. Petrisor, and M. Han, "Endocavity Ultrasound Probe Manipulators," *IEEE/ASME TRANSACTIONS ON MECHATRONICS*, pp. in Press, 2012. http://urobotics.urology.jhu.edu/pub/2012-stoianovici-tmech.pdf

[8] M. Han, C. Kim, P. Mozer, F. Schafer, S. Badaan, B. Vigaru, K. Tseng, D. Petrisor, B. Trock, and D. Stoianovici, "Tandem-robot Assisted Laparoscopic Radical Prostatectomy to Improve the Neurovascular Bundle Visualization: A Feasibility Study," *Urology*, vol. 77, pp. 502-506, 2011. http://urobotics.urology.jhu.edu/pub/2011-han-urology.pdf

[9] D. Cool, S. Sherebrin, J. Izawa, J. Chin, and A. Fenster, "Design and evaluation of a 3D transrectal ultrasound prostate biopsy system," *Med Phys*, vol. 35, pp. 4695-707, 2008.

[10] S. Xu, J. Kruecker, P. Guion, N. Glossop, Z. Neeman, P. Choyke, A. K. Singh, and B. J. Wood, "Closed-loop control in fused MR-TRUS image-guided prostate biopsy," *Med Image Comput Comput Assist Interv*, vol. 10, pp. 128-35, 2007.

[11] G. L. Andriole, T. L. Bullock, J. S. Belani, E. Traxel, Y. Yan, D. G. Bostwick, and P. A. Humphrey, "Is there a better way to biopsy the prostate? Prospects for a novel transrectal systematic biopsy approach," *Urology*, vol. 70, pp. 22-6, 2007.

[12] J. Bax, D. Cool, L. Gardi, K. Knight, D. Smith, J. Montreuil, S. Sherebrin, C. Romagnoli, and A. Fenster, "Mechanically assisted 3D ultrasound guided prostate biopsy system," *Med Phys*, vol. 35, pp. 5397-410, 2008.

[13] L. Mercier, T. Lango, F. Lindseth, and D. L. Collins, "A review of calibration techniques for freehand 3-D ultrasound systems," *Ultrasound Med Biol*, vol. 31, pp. 449-71, 2005.

[14] E. M. Boctor, A. Jain, M. A. Choti, R. H. Taylor, and G. Fichtinger, "A rapid calibration method for registration and 3D tracking of ultrasound images using spatial localizer," *Medical Imaging 2003: Ultrasonic Imaging and Signal Processing*, vol. 5035, pp. 521-532, 2003.

[15] E. Boctor, A. Viswanathan, M. Choti, R. H. Taylor, G. Fichtinger, and G. Hager, "A novel closed form solution for ultrasound calibration," *2004 2nd Ieee International Symposium on Biomedical Imaging: Macro to Nano, Vols 1 and 2*, pp. 527-530, 2004.

[16] P. W. Hsu, R. W. Prager, A. H. Gee, and G. M. Treece, "Real-time freehand 3D ultrasound calibration," *Ultrasound Med Biol*, vol. 34, pp. 239-51, 2008.

[17] R. W. Prager, R. N. Rohling, A. H. Gee, and L. Berman, "Rapid calibration for 3-D freehand ultrasound," *Ultrasound Med Biol*, vol. 24, pp. 855-69, 1998.

[18] F. Rousseau, P. Hellier, and C. Barillot, "Confhusius: a robust and fully automatic calibration method for 3D freehand ultrasound," *Med Image Anal*, vol. 9, pp. 25-38, 2005.

[19] D. Stoianovici, L. L. Whitcomb, J. H. Anderson, R. H. Taylor, and L. R. Kavoussi, "A modular surgical robotic system for image guided percutaneous procedures," presented at Medical Image Computing and Computer-Assisted Intervention, 1998. http://urobotics.urology.jhu.edu/pub/1998-stoianovici-miccai.pdf

[20] W. D. D'Souza, E. L. Madsen, O. Unal, K. K. Vigen, G. R. Frank, and B. R. Thomadsen, "Tissue mimicking materials for a multi-imaging modality prostate phantom," *Med Phys*, vol. 28, pp. 688-700, 2001.

Chunwoo Kim (S'2010) received a B.S. degree from Department of Mechanical Aerospace Engineering at Seoul National University in 2008. Since 2008, he is Ph.D. student in Urology Robotics Lab at Johns Hopkins University. He is a recipient of the Fulbright scholarship and the Prostate Cancer Research Training Award of the United States Department of Defense. His research interests include image-guided robots and medical imaging.

Doyoung Chang (S'2010) received his Ph.D. degree in Mechanical and Aerospace Engineering from Seoul National University, 2012, where he also received his B.S. degree in 2006. Dr. Chang is now a post-doctoral research fellow at the Urology Robotics Lab at Johns Hopkins University. His research interests include image guided medical robotics and bio-inspired robot design.

Doru Petrisor (ASME M'2003) received a M.S. degree in Mechanical Engineering from the University of Craiova, Romania in 1988, the PhD from the University of Petrosani, Romania in 2002, followed by a research fellowship in Urology at the Johns Hopkins University. Between 1991-1994 he was Assistant Professor at the University of Craiova and Lecturer since 1994. In 2002 he joined the Urology Robotics research group at Johns Hopkins and currently is Research Associate Professor. Dr. Petrisor's specialty is design of interventional and surgical robots, medical instrumentation, and CNC manufacturing. His bibliography includes numerous articles, presentations, and 4 patents of invention.

Gregory Chirikjian received undergraduate degrees from Johns Hopkins University in 1988, and the Ph.D. degree from the California Institute of Technology, Pasadena, in 1992. Since 1992, he has been on the faculty of the Department of Mechanical Engineering, Johns Hopkins University, where he is now professor. From 2004-2007 he served as department chair. His research interests include robotics, applications of group theory in a variety of engineering disciplines and the mechanics of biological macromolecules. He is a 1993 National Science Foundation Young Investigator, a 1994 Presidential Faculty Fellow, and a 1996 recipient of the ASME Pi Tau Sigma Gold Medal. He is a Fellow of the ASME and IEEE, and author of more than 200 publications, including three books.

Misop Han MD, MS received his undergraduate, medical school, and urology training at the Johns Hopkins University, Baltimore, MD. He is Associate Professor of Urology and Oncology at the James Buchanan Brady Urological Institute, Johns Hopkins Medicine. His main clinical focus is in urological oncology with a special emphasis in prostate cancer and kidney cancer. His research interests include the outcome of radical prostatectomy and image-guided surgery using surgical robots. He has published extensively in these subjects.

Dan Stoianovici (ASME M'1994) received the Ph.D. degree from Southern Methodist University, Dallas, TX, in 1996. He is Professor of Urology, Mechanical Engineering, and Neurosurgery at the Johns Hopkins University. He is also the Director of the Urology Robotics Program. His specialty is medical robotics in particular robotic hardware and image-guided robots. He serves on the editorial boards of the IEEE/ASME TRANSACTIONS on Mechatronics, Journal of Endourology, International Journal of Medical Robotics and Computer Aided Surgery, the British Journal of Urology International and other medical-engineering journals.